electronics

MDPI

Article

Liquid Crystal-Filled 60 GHz Coaxially Structured Phase Shifter Design and Simulation with Enhanced Figure of Merit by Novel Permittivity-Dependent Impedance Matching

Jinfeng Li [1,2,3,*] and Haorong Li [1]

[1] Beijing Key Laboratory of Millimeter Wave and Terahertz Technology, School of Integrated Circuits and Electronics, Beijing Institute of Technology, Beijing 100081, China
[2] Advanced Research Institute of Multidisciplinary Science, Beijing Institute of Technology, Beijing 100081, China
[3] Department of Electrical and Electronic Engineering, Imperial College London, London SW7 2AZ, UK
* Correspondence: jinfengcambridge@bit.edu.cn or jinfeng.li@imperial.ac.uk

Abstract: This work serves as the first simulation investigation to tackle the liquid crystal (LC)-filled coaxially structured continuously variable phase shifter at 60 GHz, wherein the LCs act as single tunable dielectrics fully occupying the millimeter-wave (mmW) power transmitted (i.e., free of leakage or interference). Impedance and effective dielectric constant computations are settled, followed by the quantification of the interplay between the dielectric thickness and the dielectric constant (Dk) for a controlled 50 Ω impedance. Geometry's aspect ratio (AR) effects are exploited for the coaxially accommodating topology filled with mmW-tailored LCs with an operatable Dk range of 2.754 (isotropic state) to 3.3 (saturated bias state). In addition to the proposed structure's noise-free advantages, a novel figure of merit (FoM) enhancement method based on Dk-selection-based impedance matching is proposed. The optimum FoM design by simulation exhibits a 0–180.19° continuously variable phase shift with a maximum insertion loss of 1.75871 dB, i.e., a simulated FoM of 102.46°/dB when the LC-filled coaxial geometry is 50 Ω and matched with the Dk of 2.8, corresponding to the dielectric thickness of 0.34876 mm and line length of 15.92 mm. The envisioned device fabrication and assembly processes are free of the conventional polyimide alignment agent and the related thermal and electrical concerns. Significant cost reduction and yield improvement can hence be envisaged. The topology can also serve as a test structure for broadband characterizations of LC materials and new electro-optical effects.

Keywords: microwave; millimeter-wave; phase shifter; insertion loss; figure of merit; coaxial; delay line; liquid crystal; impedance matching; dielectric loss; conductor loss; 60 GHz

check for updates

Citation: Li, J.; Li, H. Liquid Crystal-Filled 60 GHz Coaxially Structured Phase Shifter Design and Simulation with Enhanced Figure of Merit by Novel Permittivity-Dependent Impedance Matching. *Electronics* **2024**, *13*, 626. https://doi.org/10.3390/electronics13030626

Academic Editors: Md. Shamim Ahsan, Ahmed Jalal, Mohammad Rakib Uddin and Mohd Rashidi Che Beson

Received: 13 December 2023
Revised: 26 January 2024
Accepted: 31 January 2024
Published: 2 February 2024

1. Introduction

In recent decades, a surge of interest has been registered in the electronically reconfigurable microwave (MW) [1] and millimeter-wave (mmW) [2] components with low power consumption [3] and nonmechanical movements [4]. This is due to the growing demand for flexible and adaptable MW and mmW systems for use in both communications [5–8] and noncommunication applications [9,10], as illustrated by Figure 1 below.

The targeted reconfigurable modality of either phase (e.g., wavefront phase control for beam steering [11]), frequency (e.g., tunable resonance for band-pass, band-stop filters [2], and spatial filtering such as frequency-selective surfaces [12]), amplitude (for variable attenuation [13]), or polarization (e.g., smart antennas [14,15]) is envisaged to be adaptively modulated to meet the dynamically changing requirements of agile environments or applications. In the context of the increasingly congested frequency spectrum and complicated systems, reconfigurability is thus highly sought after (or mandatory in the future electronics

roadmap) to achieve increased system efficiency, improved performance, and reduced time (and cost) on development and maintenance.

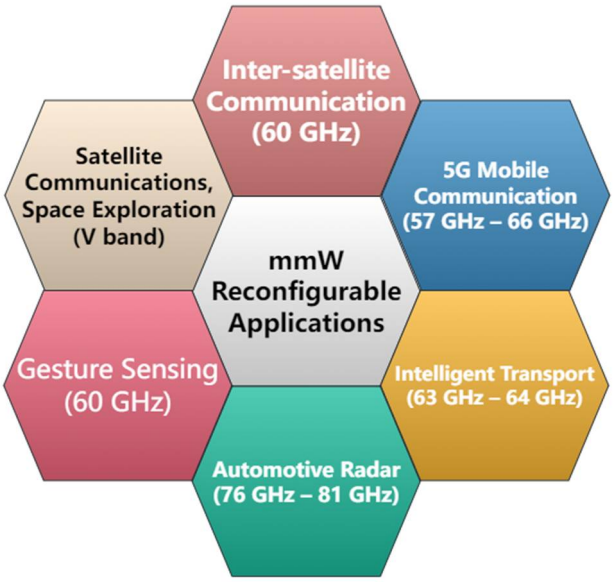

Figure 1. Illustration of mmW reconfigurable applications (60 GHz and beyond).

Reconfigurable MW components (e.g., phase shifters [16,17]) are designed to be dynamically adjustable, allowing them to change their electrical characteristics (e.g., wave speed and output signal phase) in response to changing modalities (e.g., temperatures, electric fields, magnetic fields, and light intensity). This is conventionally achieved through the use of active or passive components, such as MEMS (microelectromechanical systems) [2], varactors [18], or solid-state switches (e.g., p-i-n diodes [6], field effect transistors), wherein the high-precision structure patterning for higher frequencies can resort to state-of-the-art micro- [19] and nanomachining [20,21] techniques. These devices are ultra-fast responders, but their resolution is limited spatially (e.g., limiting the accuracy of beam steering angles).

Liquid crystals (LCs) in the nematic phase [22] are remediating this spatial resolution challenge due to their continuous tunability [23], which is subjective to external stimuli, e.g., low-frequency low-amplitude electric voltage bias (of low power consumptions) for our enclosed coplanar waveguide phase shifter filled with LCs [24] or high-current-driven magnetic bias (of higher power consumptions) for certain metallic waveguides [25] and, more recently, dielectric waveguide-based topologies [26] that accommodate LCs. The nanoscopically molecular orientations of LCs can be macroscopically represented by directors [22,27] that are controllable by these external stimuli (electric, magnetic, temperature, or deformation fields). Fundamentally, their molecular shape anisotropy [24] and the resulting produced variable dipole moments can be exploited to develop a variable dielectric constant (dependent on the interacted field direction) for reconfigurable phase and wavefront steering applications (e.g., tunable filters [28], variable phase shifters [29], tunable antennas [30], and antenna arrays [31]). Arguably, the 5G/6G, IoT, vehicle, and satellite markets are becoming growth engines for the LC mmW industry.

In realizing these applications, how to accommodate LCs (liquid-like dielectric with fluidity) in a suitable transmission line (or waveguide) structure (with low insertion loss and a high tuning range) is of research interest. However, the status of LC mmW components is still primarily limited to planar, low-speed tuning applications. New methods and structures should be in place to increase their acceptance in wider scenarios targeting wider stakeholders. Pondering about the year just past, we proposed a novel, partially shielded coplanar waveguide with metasurfaces for LC phase shifters beyond 67 GHz [32], 79 GHz meandering enclosed coplanar variable delay lines in LCs encapsulated within independent and shared cavities [33], and a 60 GHz 0–360° passive analog delay line in

LC technology based on a novel conductor-backed fully enclosed coplanar waveguide [34]. These structures are compact and planar (semi-planar) in nature, meaning that the core line is semi-open or partially open and, hence, is vulnerable to electromagnetic interference (crosstalk) [35], higher-order modes [24], noises, and related unstable problems [36] that can compromise the device's performance and reliability, in particular at higher-frequency mmW regimes.

The classically established coaxial structure, featuring a fully enclosed core line (i.e., anti-interference), however, is seldom reported in the use for LC MW or mmW components. The coaxial transmission line structure features excellent shielding against electromagnetic interference (EMI). Furthermore, the fully enclosed metal housing also provides mechanical stability, making them well suited for use in harsh environments. The combination of the coaxial structure with the tunable LCs is arguably a novel approach to phase shifting. By quantifying the performance (advantages and limitations) of this type of device using Ansys HFSS (a high-frequency structure simulator in version 2022 R1), the simulated evaluation to be reported for the first time in this work will provide important insights into its behavior, which can be used to optimize the design of the device and improve its performance for reconfigurable mmW applications.

2. Materials and Methods

2.1. Tuning Mechanisms and Tuning States Investigations

Macroscopically, the tuning mechanism of the phase shifter is illustrated by our device prototype of an LC-filled enclosed coplanar waveguide (ECPW) delay line [24] shown in Figure 2. Note that the conveyance of low frequency (LF) bias voltage signal is along the same signal path as the radio frequency (RF) signal to be transmitted. To avoid the possibly disruptive effect of the LF (DC) bias going further down the RF path (e.g., towards the vector network analyzer for device characterization or towards an antenna radiator in a phased array system), a pair of three-port bias tees (e.g., models from Picosecond Pulse Labs or equivalent vendors encompassing a coaxial bias insertion tee and DC blocking capacitor inside the block) can be implemented accordingly to decouple the mixed signals, thus ensuring that the targeted RF signal output path is free of the LF bias component.

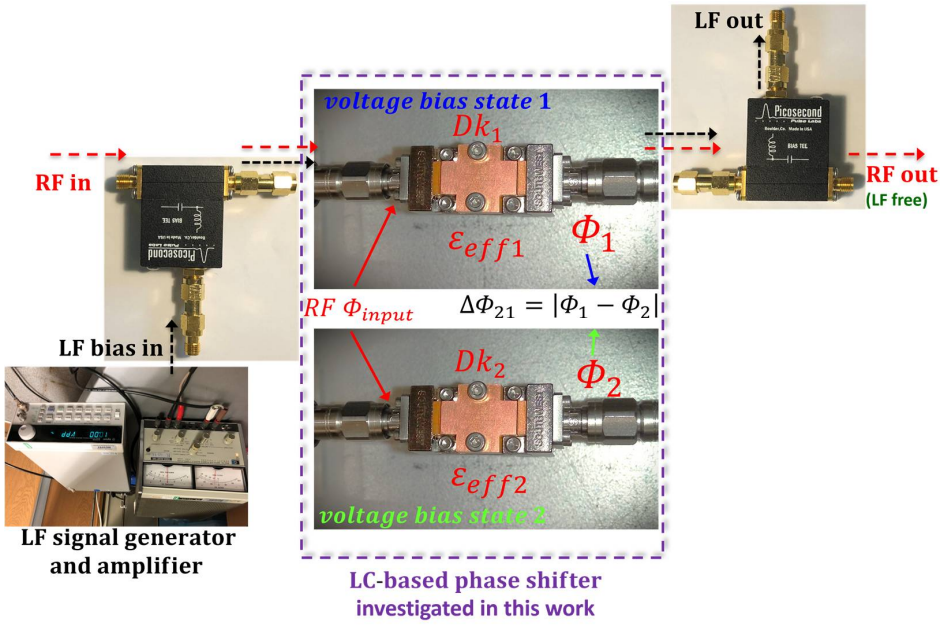

Figure 2. Differential phase shifting principle illustrated by our previously fabricated demonstration of an LC-filled ECPW 0–180° variable delay line (phase shifter) device [24] with mixed signals of RF (for transmitting) and LF (for LC biasing) decoupled by bias tees.

To distinguish the two signals (LF and RF) in Figure 2 for ease of understanding, lines and characters in red represent the RF signal to be transmitted, while the flow of the LF voltage bias is denoted in black. Note that the real device shown in Figure 2 (with measured performance documented in [24]) is for illustration purposes only, i.e., without indicating any measurement results to be reported from the current simulation-only study into the LC-filled coaxial structure in this work.

Looking analytically into the standalone LC-based phase shifter itself (as bounded by the dashed box in purple from Figure 2 above), the obtained differential phase shift $\Delta\Phi_{21}$ is mathematically governed by Equation (1), where c is the speed of light, f is frequency, L is the length of the delay line, and ε_{eff1} and ε_{eff2} are the two states of the effective dielectric constant induced by diverse bias voltages, respectively.

$$\Delta\Phi_{21} = \omega\Delta t = \frac{2\pi fL}{c}|\sqrt{\varepsilon_{eff1}} - \sqrt{\varepsilon_{eff2}}|. \quad (1)$$

Similar equations have been reported extensively in a majority of papers [26,29] concerning LC-based mmW phase shifting devices, whereas very seldom does it fundamentally understand the quintessence underpinning the tuning problem, i.e., the distinction between the tuning range (tunability) of LC materials and the tuning range of the whole delay line (phase shifter) device. As such, the concept of wave-occupied volume ratio (colloquially referred to as mmW power concentration ratio) between tunable dielectrics and nontunable dielectrics was first theorized in our past works on multidielectric-encompassing delay line systems (e.g., inverted microstrip [29], floating-electrode-free coplanar [37], and enclosed coplanar [24]), which demystifies the distinction between a device's tuning range and a materials' tunability. Compared to our established LC-based inverted microstrip [29] or enclosed coplanar waveguide phase shifters [24] that encompass multiple dielectrics (i.e., LCs as tunable dielectrics and a PCB as a nontunable dielectric), the LC-filled coaxial phase shifter proposed in this work is arguably a single-dielectric delay line (signal propagating purely in LC tunable dielectrics without the nontunable dielectric PCB part), with LCs entirely enclosed by two concentric spherical conductors (core line and outer housing).

In this work, the core line geometry of the proposed coaxial delay line is as per the state-of-the-art, commercially available 1.85 mm coaxial connectors tailored for 60 GHz and beyond to minimize geometry discontinuity and related higher-order modes, i.e., with the core line's diameter measuring 0.009 inch (0.23 mm). The dielectric material filling the coaxial cavity is the GT3-24002 type of LC with the material's dielectric constant maximally characterized as 3.3 [17] at the saturated bias state (i.e., denoted as $Dk_{\parallel}$ for the molecular directors in parallel with the mmW polarization), with the corresponding dissipation factor ($DF_{\parallel}$) reaching its lowest point of 0.0032 at 60 GHz [24].

Note that the minimally achievable $Dk_{\perp}$ of 2.5 (with $DF_{\perp}$ reaching a highest point of 0.0123) [24] for planar transmission line structures (wherein the planar alignment of polyimide is well established) does not apply to the proposed coaxial structure due to the technically demanding task of mechanically rubbing a radial (nonplanar) structure to produce surface-anchoring-based pre-alignment (discussed later in Sections 3.3 and 4). As such, the coaxial approach will be free of mechanical rubbing (pre-alignment treatment) and functions purely on an electrical bias field. Upon removal of the voltage bias (or reducing it below the Fredericks transition threshold [22,24]), the Dk state of the LCs will be homogeneous and isotropic-like (Dk_{iso}), which can be mathematically described by Equation (2) for uniaxial nematic LC molecules that are anisotropic.

$$\sqrt{Dk_{iso}} = \frac{\sqrt{Dk_{\parallel}} + \sqrt{Dk_{\perp}} \times 2}{3}, \quad (2)$$

where Dk_{iso} denotes the dielectric constant of LCs derived at the isotropic state, $Dk_{\parallel}$ denotes the dielectric constant of LCs at the saturated bias state (directors reoriented in parallel with the mmW polarization), and $Dk_{\perp}$ represents the dielectric constant of LCs at

another extreme state with directors perpendicular to the mmW polarization. For the GT3-24002 grade of LCs employed, Dk_{iso} can be derived as 2.754 as per our past experimental characterization knowledge of $Dk_{||}$ = 3.3 and $Dk_{\perp}$ = 2.5 for V band (60 GHz) [17]. Similarly, the dissipation factor at the isotropic state (DF_{iso}) is derived as 0.0111.

Note that we do not intend to utilize the conventionally complex and power-consuming magnetic-driving approach for the LCs pre-alignment (as adopted by LC waveguides [25]). Instead, we rely purely on the isotropic state of the LCs (free of rubbing-based pre-alignment) as one of the extreme states, which simplifies the fabrication (reduced cost) and enables low-power control with ease, albeit at the cost of partially compromising the operational range of Dk (from 2.754 to 3.3) as compared to planar structures with the fully exploited range of Dk (from 2.5 to 3.3) for the same LC material (GT3-24002). The experimentally characterized dielectric properties are shown in Figure 3, with the analytical working range of Dk highlighted from 2.754 (isotropic state) to 3.3 (saturated bias state as sketched, wherein the LC directors are fully in line with the mmW polarization at 60 GHz) and the nonoperational range of Dk from 2.5 to 2.754.

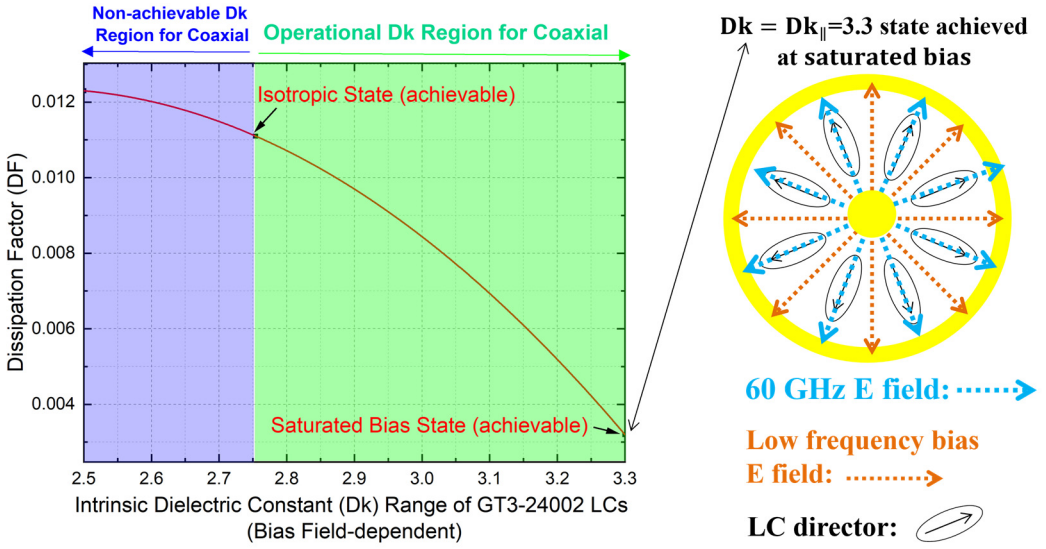

Figure 3. Dielectric characterization of LCs (GT3-24002) by experiments and their theoretically operational tuning states achievable in our proposed coaxial delay line structure at 60 GHz.

2.2. mmW Power-Occupying Volume Ratio in Tunable Dielectrics

Despite the truncated (reduced by almost a half) tuning (working) range of the LCs, the proposed coaxial structure exhibits its own advantage in terms of the mmW power-occupying volume ratio (mmW-PoVR) in the tunable dielectrics, as compared with the multidielectric type of topology that encompass other nontunable dielectrics (e.g., inverted microstrip and coplanar-related structures, as mentioned earlier, that include PCB substrates that are not tunable). The significance of mmW-PoVR was first raised by us [24,37] and was evidenced in our enclosed coplanar waveguide [24] and inverted microstrip line [29] phase shifter prototypes, where the mmW signal being transmitted was partially occupying the tunable dielectrics (LCs), whereas another portion is dissipated in nontunable regions (i.e., PCB substrate). From the deviation between the LC material's intrinsic figure of merit (FoM) [17] and the delay line device's FoM [11] observed in our previous analysis, we have identified that the mmW-PoVR can enhance or degrade the overall tunability (operational tuning range) of the phase shifter device.

For the coaxial topology proposed in this work, 100% of the mmW-PoVR in the part of the tunable dielectrics can be theoretically idealized (due to the fully enclosed nature of the topology). As such, the effective permittivity of the transmission line can be equivalent to the Dk of the filled LCs (macroscopically), as illustrated in Figure 3 shown earlier for the fully saturated state where LC molecular directors align with the polarization radially. To facilitate

a wider comparison with other topologies of multidielectrics, we push our mmW-PoVR definition further by quantifying it without loss of generality in Equations (3) and (4):

$$\Delta\varepsilon = |\varepsilon_{\text{eff}} - \text{Dk}_{\text{LC}}|, \tag{3}$$

$$\text{mmW} - \text{PoVR} = \left(1 - \frac{\Delta\varepsilon}{\text{Dk}_{\text{LC}}}\right) \times 100\%, \tag{4}$$

where ε_{eff} denotes the effective permittivity of the device, and Dk_{LC} is the dielectric constant of LCs operated in the device. Note that ε_{eff} is intricately dependent on the device's geometry (e.g., the thickness of the LCs) and the materials (LCs and other dielectrics, if any) at a specific frequency. As discussed above, the ε_{eff} and Dk_{LC} are theoretically idealized as equal, hence the 100% mmW-PoVR. To verify this idealization, we also conduct full-wave simulations in Section 3.1 to quantify the $\Delta\varepsilon$ and mmW-PoVR numerically.

Excitingly, the idealized 100% mmW-PoVR in the tunable dielectrics of the coaxial structure implies a maximumly achievable transfer rate of a wave-guiding (transmitting) device structure that fully transfers the tuning capability of tunable dielectrics (i.e., LCs in this work) to the differential phase shift of the phase shifter device. As such, the unique advantage of the coaxial topology in the mmW-PoVR may tip the balance and enable it to compete with (or even outperform) established planar solutions in LC-based phase shifters (inverted microstrip [29] and coplanar-adapted structures [24,32–34]). To answer this interesting question, the results of the performance evaluation and comparison are presented in Sections 3.3 and 3.4 based on the standalone device evaluations without the external bias tees. How the decoupling network can perturb the differential phase shift and insertion loss will be investigated in future experimental endeavors, as discussed in Section 3.4.

Note that the methodology proposed here (from Sections 2.2–2.5) is not only targeting a simplified yet accurate design process but is also embedding our strategic thinking rooted in device physics for maximizing the possibility of obtaining an enhanced performance, for which we raised the unconventional concept of mmW-PoVR (Section 2.2), investigated the aspect ratio effect (Section 2.3), proposed the novel Dk-dependent impedance matching baseline approach (Section 2.4), and implemented the dissipative loss decomposition analysis (Section 2.5).

2.3. Cross-Sectional Geometry Investigations through the Lens of Aspect Ratio

In the optimization roadmap of LC-based tunable mmW devices, material dielectric response and the device structure (geometry) have played a big part. Notably, the advancement of material synthesis by molecular mechanism innovation has been incremental and cost-prohibitive, whereas the room for the device's geometry optimization remains vast and relatively inexpensive. While the variation of a single parameter in a transmission line geometry could tip the balance of the device's overall performance, it is more fundamentally an aspect ratio-inspired problem for most two-dimensional (2D) geometries (where the critical features lie in the 2D cross-section, and the propagating statistics happen along the line length, which is integrated).

The first attempt at capturing the aspect ratio (AR) effect was reported in [37] for our designed 60–90 GHz fully symmetric coplanar waveguide (CPW) phase shifter with LCs filled into the two symmetric channels, characterized by the aspect ratio of the LCs' thickness (T_{LC}) to the channel width (W_{gap}), as depicted in Figure 4.

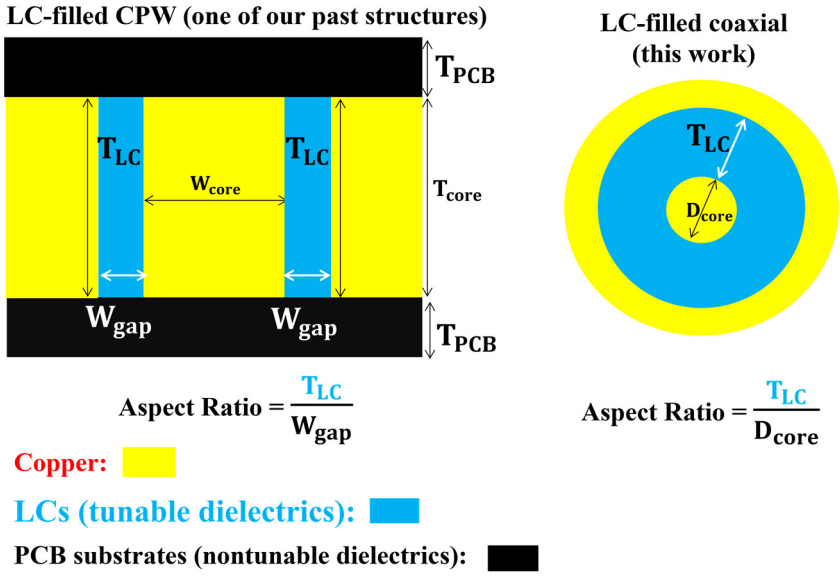

Figure 4. Geometry aspect ratios (AR) identified for our LC-filled CPW phase shifter [37] and LC-filled coaxial delay line model (this work).

For LC-based variable delay lines, it is crucial to maintain a consistent impedance along the length of the line for optimal signal transmission. The aspect ratio influences the characteristic impedance of the coaxial line. Altering the dimensions changes the capacitance and inductance per unit length, impacting the impedance and hence the signal integrity and reflections. Equation (5) represents the characteristic impedance (Z_0) of a coaxial transmission line with an inner core line diameter of D_{core}, an LC dielectric thickness of T_{LC}, and an LC dielectric constant of Dk_{LC}.

$$Z_0 = \frac{60}{\sqrt{Dk_{LC}}} \ln\left(\frac{D_{core} + 2T_{LC}}{D_{core}}\right). \tag{5}$$

Given a controlled characteristic impedance of Z_0 = 50 Ω, Equation (5) can be rearranged to Equation (6) below:

$$T_{LC} = D_{core}\left(e^{\frac{5\sqrt{Dk_{LC}}}{6}} - 1\right)/2. \tag{6}$$

Note that Equation (6) can be further arranged as the geometry aspect ratio (AR) of T_{LC} to D_{core} in Equation (7) below:

$$AR = \frac{T_{LC}}{D_{core}} = 0.5\left(e^{\frac{5\sqrt{Dk_{LC}}}{6}} - 1\right). \tag{7}$$

In this work, the coaxial AR effect parameterized with the Dk of the LCs is quantified in Section 3.1 for 50 Ω maintained LC-filled coaxial delay lines at 60 GHz.

2.4. Novel Impedance Matching Baseline Method for FoM Enhancement

In the optimization roadmap of LC-based mmW tunable phase shifters, one of the grand challenges is producing the required phase shift (e.g., 0–180°) within the insertion loss limit (e.g., <2 dB [29]), for which the metric of figure of merit (FoM) is widely accepted to take into account both the maximally achievable phase shift ($\Delta\Phi_{max}$) and maximally induced insertion loss (IL_{max}), as mathematically shown in Equation (8) below:

$$FoM = \frac{\Delta\Phi_{max}}{IL_{max}}, \tag{8}$$

where $\Delta\Phi_{max}$ is calculated by differentiating the two achievable extreme states of the effective permittivity at a specific frequency (e.g., 60 GHz), and the IL_{max} computation is performed by identifying the highest insertion loss among all tuning (biasing) states at the same frequency. From our past research and experimental results into the multidielectric type of LC-filled phase shifter [11,24], the IL_{max} primarily happens at the lowest operational Dk state, where the dissipation factor (DF) of the LCs is at its maximum (as characterized in Figure 3 in Section 2.1).

In this work, we propose and carry out a novel dynamic Dk matching approach for advancing the frontiers of our knowledge into an LC-filled single-dielectric delay line system (i.e., coaxial phase shifter). By parametrizing the Dk baseline for a perfectly matched impedance (50 Ω), the resultantly induced, diversely corresponding T_{LC} (for each Dk baseline) can affect the electric field intensity distribution, hence perturbing the metal and dielectric losses (surface and volume integral ones, respectively) as well as the phase tuning range (mmW-PoVR as discussed above). The T_{LC} here underpins twofold significance. For the conductor loss, T_{LC} represents the distance between the two conductors (core line and grounding housing) to impact the intensity of the electric (E) field (in particular the E field peaking at the edges of the core line). For the dielectric loss, T_{LC} indicates the thickness of the tunable dielectrics, which not only impacts the E field intensity (distribution and peaking, etc.) but also affects the volume of the dielectrics (volumetric loss).

By way of illustration, we show our simulated insertion losses of a 1 mm long coaxially structured LC delay line from 54 GHz to 66 GHz for the two extreme bias states plotted in the same graph, i.e., isotropic state (Dk_{iso} = 2.754, DF_{iso} = 0.0111) and saturated bias state ($Dk_{||}$ = 3.3, $DF_{||}$ = 0.0032). Two designs are shown and compared, i.e., Figure 5a on a geometry with 50 Ω impedance matched at the saturated biased Dk = 3.3 state (corresponding to T_{LC} = 0.41 mm) versus Figure 5b on another geometry that is 50 Ω impedance matched at the isotropic Dk = 2.754 state (corresponding to T_{LC} = 0.34 mm). Both designs are 1 mm in length, differing in the T_{LC} due to the different Dk matching baselines chosen.

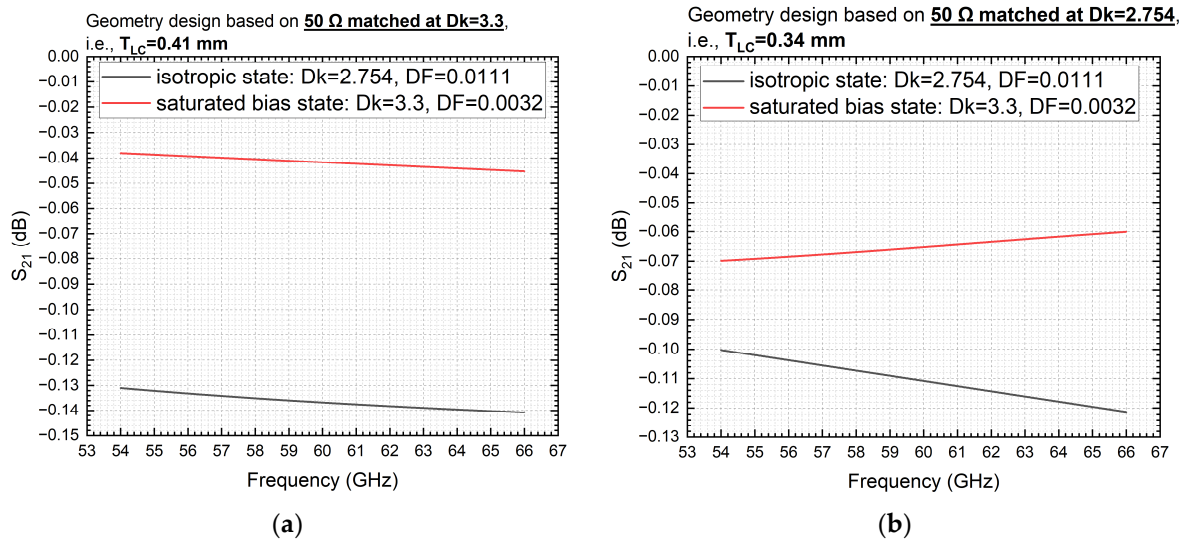

Figure 5. Simulated insertion loss of 1 mm long coaxial delay line filled with LCs: (**a**) cross-section design with T_{LC} = 0.41 mm for 50 Ω matched at Dk = 3.3 state; (**b**) cross-section design with T_{LC} = 0.34 mm for 50 Ω matched at Dk = 2.754 state.

From Figure 5b above, concerning the results of the 1 mm long coaxial delay line's cross-sectional geometry design (i.e., T_{LC}) with its impedance perfectly matched at the Dk state of 2.754 (isotropic state of LCs), we observe that its insertion loss for the Dk = 3.3 state (wherein the LCs are fully biased to the saturated status) is contrarily reducing with frequency, as compared with the majority of situations (i.e., insertion loss increases with frequency).

This unconventional behavior is due to the return loss (impedance mismatching) that dominates the total dissipation, which contributes to the elevated insertion loss of the specific frequencies. As evidenced by our simulated return loss in Figure 6a compared with Figure 6b (representing the design from perfectly matching to least matching for the Dk = 3.3 bias state), there is a significant increase in S_{11} (return loss) by approximately 30 dB for the saturated bias state (Dk = 3.3).

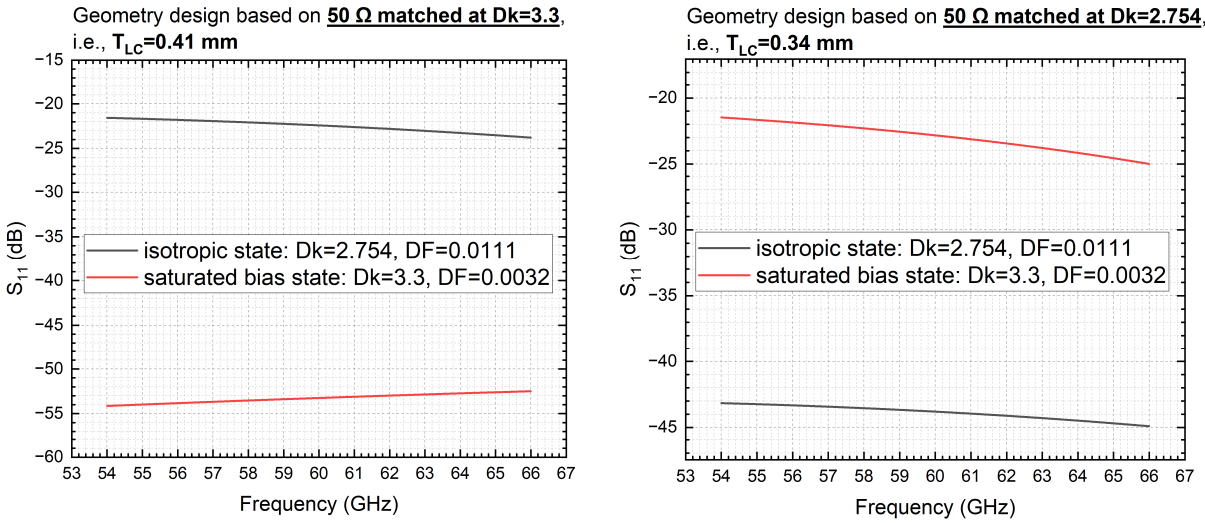

Figure 6. Simulated return loss of 1 mm long coaxial delay line filled with LCs: (**a**) cross-section design with T_{LC} = 0.41 mm for 50 Ω matched at Dk = 3.3 state; (**b**) cross-section design with T_{LC} = 0.34 mm for 50 Ω matched at Dk = 2.754 state.

The reason for this domination of the return loss is that the 1 mm length for the loss density integration contributes relatively little to the LC volumetric loss and metal losses. In summary, deciding which geometry design matched which Dk of the LCs (which determines the required T_{LC}) is arguably an optimization problem, as it can drastically impact the device's performance and even tip the balance of the frequency response, i.e., return loss can dominate over dielectric and metal losses. As such, we investigate the optimum Dk matching baseline in this work as a novel method for enhancing the overall FoM of the LC-filled phase shifters at 60 GHz. The optimization results for a 0–180° phase shifter will be reported in Section 3.3. Furthermore, we propose a loss decomposition analysis approach in the following Section 2.5 to quantify each loss component (dielectrics and metals).

2.5. Loss Components Decomposition Analysis

Experimental measurements via a vector network analyzer (VNA) can provide transmitted and reflected power information, wherein the insertion loss (IL) and return loss (RL) are obtained. Nevertheless, these fail to convey the specific loss dissipated in the materials composed, i.e., conductor loss, dielectric loss, radiation loss, etc. Instead, in silico analysis by full-wave simulations enables us to understand each loss element with unprecedented detail, i.e., not only the total conductor loss and dielectric loss can be identified but also the detailed power dissipated on the core line's outer surface, the outer conductor's inner surface, and the LC volume can be quantitatively specified, respectively.

Based on our established loss characterization study for the LC-based inverted microstrip [29] and enclosed coplanar waveguide [24], transferrable approaches are applied to decompose the loss elements of the LC-filled coaxial delay line proposed in this work. The phasor form of the conductor loss and dielectric loss per unit length (i.e., cross-sectional study) is theoretically derived using a cylindrical coordinate (r, ∅) in Figure 7, wherein

r = 0 denotes the center of the core line, $r = D_{core}/2$ represents the surface of the core line, and $D_{core}/2 < r < D_{core}/2 + T_{LC}$ indicates the enclosed (filled) LC region.

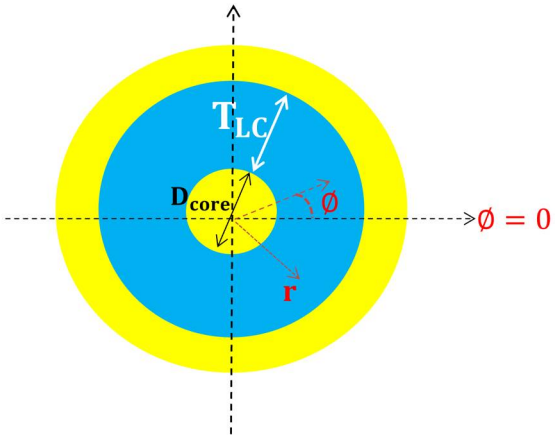

Figure 7. Cylindrical coordinate employed for the cross-section of our LC-filled coaxial delay line model. Conductors are denoted in yellow, and the filled LC region is depicted in blue.

As such, the phasor form for the core line's ohmic conductor loss per unit length ($P_{core_{s_0}}$), as well as the outer conductor's conductor loss per unit length ($P_{housing_{s_0}}$), is derived in Equations (9) and (10) below, respectively, where σ denotes conductivity and μ denotes permeability.

$$P_{core_{s_0}} = {I_{s_0}}^2 R = \left[\int_{r=\frac{D_{core}}{2}} \int_{\varnothing=0}^{\varnothing=2\pi} \sigma E_s(r,\varnothing)_0 d\varnothing dr\right]^2 \times \frac{\sqrt{\pi f \sigma \mu}}{\sigma \pi D_{core}}, \quad (9)$$

$$P_{housing_{s_0}} = \left[\int_{r=\frac{D_{core}}{2}+T_{LC}} \int_{\varnothing=0}^{\varnothing=2\pi} \sigma E_s(r,\varnothing)_0 d\varnothing dr\right]^2 \times \frac{\sqrt{\pi f \sigma \mu}}{\sigma \pi (2T_{LC} + D_{core})}. \quad (10)$$

As per the transferrable experience from our past LC loss dissipation analysis on the enclosed coplanar [24] and coplanar waveguides [37], the phasor form for the LCs' dielectric loss per unit length ($P_{LC_{s_0}}$) of the LC-filled coaxial delay line in this work is derived in Equation (11) below:

$$P_{LC_{s_0}} = 2\pi f \varepsilon_0 Dk_{LC} DF_{LC} \int_{r=\frac{D_{core}}{2}}^{r=\frac{D_{core}}{2}+T_{LC}} \int_{\varnothing=0}^{\varnothing=2\pi} \left|\vec{E_s}(r,\varnothing)_0\right|^2 d\varnothing dr. \quad (11)$$

Based on the cross-sectional phasor forms, the total loss of the entire device takes the integral operations on the line length, for which full-wave simulation using an HFSS (high-frequency structure simulator) is employed to quantify our analytically derived power dissipation of conductors (by surface integral) and dielectrics (by volume integral) for our LC-filled coaxial delay line.

2.6. Development Procedures and Protocols

The overarching target of this work is to modulate the 60 GHz signals with low levels of losses and decent tunability in the phase shift (per unit length or unit weight), making it well suited for real-world applications, e.g., mmW instrumentation and communication systems. The technical routes we developed encompass the aforementioned mathematical and computational framework as well as other physics-inspired work packages, commencing on characteristic impedance, effective dielectric constant, and hence the mmW-PoVR characterizations, followed by the deployment of the proposed novel Dk-dependent impedance matching approach and the loss decomposition analysis for obtaining optimum performance properties of phase shifting and insertion loss, concluded by the comprehensive performance metrics (FoM and beyond).

From the phase tuning perspective, the optimization is arguably dealing with the competition among the mmW-PoVR (advantageous for the device's tuning capability per unit length), the truncated Dk tuning range available (disadvantageous for the device's tuning capability per unit length), and the resultantly derived line length for realizing a required phase shift function. From the insertion loss perspective, the optimization roadmap has been detailed in Sections 2.4 and 2.5 regarding the competition among various loss components dissipated on metal surfaces and consumed in the dielectric volume of LCs.

Phase depths (maximum phase tuning ranges) of 0–180° are targeted as proof-of-concept (e.g., for use in intelligent reflecting surfaces [7,38]). By capturing the necessary line length in accordance with a fixed phase shift requirement (i.e., 180°), the corresponding maximum insertion loss is derived. This approach is useful to rule out the deficiency of the FoM metrics with diverse line lengths. However, it is challenging to formulate a fair comparison with other people's work that measured and reported different line lengths, different frequencies, and different phase shifting ranges, etc. As such, the results benchmark and performance comparison are conducted at the same designed frequency (i.e., 60 GHz) and phase shifting range (i.e., 0–180°) for diverse LC-filled delay line topologies, as will be presented and discussed in Section 3.4.

3. Simulation Results and Discussions

3.1. Impedance Calculations and Aspect Ratio Effects

The molecular shape anisotropy of LCs not only induces variable dipole moments for the electric permittivity variation but also causes the characteristic impedance of the device to be variable (bias-dependent). As such, it is essential to gain a comprehensive grasp of the impedance calculations. The obtained characteristic impedance (Z_0) at 60 GHz is plotted in a contour map parameterized with LCs' dielectric thickness (T_{LC}) and LCs' dielectric constant (Dk_{LC}) in Figure 8 below, with the core line's diameter fixed at 0.23 mm (for interfacing typical V band connectors at both terminals).

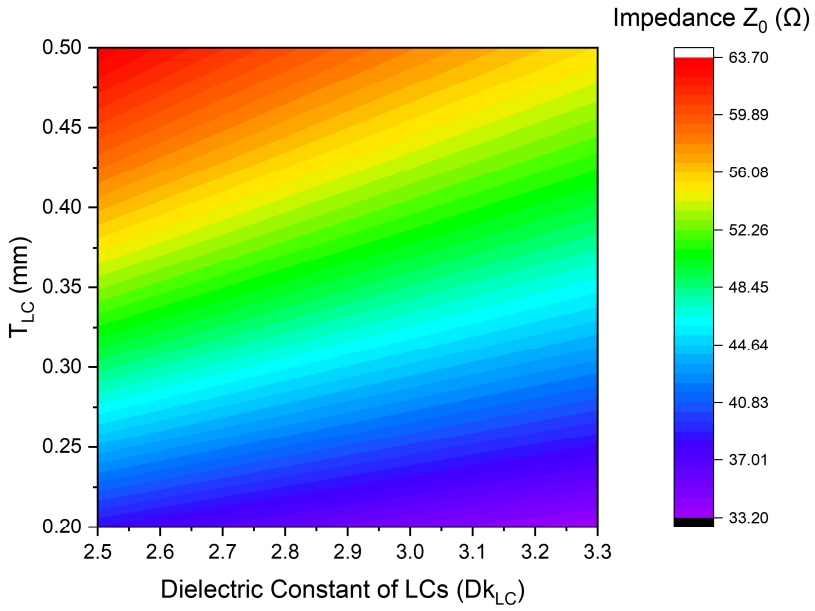

Figure 8. Characteristic impedance parametrized with LCs' thickness (T_{LC}) and dielectric constants (Dk_{LC}) for our LC-filled coaxial phase shifter model at 60 GHz.

From Figure 8, the required LCs' thickness (T_{LC}) is increasing with the LCs' dielectric constant (Dk_{LC} ranging from 2.5 to 3.3) for a controlled impedance of 50 Ω. The required elevation of T_{LC} has significant implications for both the performance (insertion loss [29], phase shifting capability [37], response time [39], and power consumption [40]) and the

device's manufacturability [36], as per our past semi-empirical studies and experimental results [11,24]. Arguably, the rising of T_{LC} mitigates the peaking for electric field intensity, hence reducing both the phase shifting capability and the insertion loss (in particular reducing the conductor loss as evidenced by [29]). The overall FoM (i.e., the ratio of the maximally achievable differential phase shift to the maximally observed insertion loss) normally rises with T_{LC} first and then levels off (as observed from [24] at 140 μm, for example). With the further increase in T_{LC}, however, not only does the enhancement in the FoM become incremental or even compromising, but it also incurs power consumption concerns (biasing voltage can drastically increase beyond a hundred volts [25]), manufacturability issues (technically demanding to maintain the flatness of the LCs' layer sandwiched between conductors), and most notably, the drastically increased response time problem (due to a loss of the mechanical anchoring by the polyimide alignment that acts as the key enabler for LCs' reorientation once removal from voltage bias). Thereby, the results in Figure 8 provide a design guideline for coaxially structured LC delay lines in terms of the LCs' selection, i.e., a lower Dk_{LC} arguably contributes to a faster tuning speed of the device, albeit at the risk of elevating the insertion loss.

If we view the results of Figure 8 from the lens of aspect ratios (AR) of T_{LC} to D_{core}, we obtain a quasilinear relationship between AR and Dk_{LC} (between 2.5 and 3.3 in this work), as observed in the zoom-in view of Figure 9a below. Instead of the requirement on increasing T_{LC} with Dk_{LC}, Figure 9a indicates that it is the AR that matters instead of the pure dependence on T_{LC}. This finding inspires a new way to drastically improve the coaxial-type LC device's tuning speed, i.e., by reducing D_{core} without increasing T_{LC}, AR will rise and satisfy the impedance matching constraint. To test the validity of this for a wider range of Dks (not necessarily LCs), Figure 9a presents the extended view of AR vs. Dk for Dks up to 50. Interestingly, the relationship between AR and Dk becomes nonlinear, and the nonlinearity becomes more significant with the increases in Dk (upwardly concave), as evidenced by Figure 9b, produced by taking a second-order derivative of the curve from Figure 9a. This indicates that the further increase in Dk (material selection problem) is detrimental to the device's fabrication feasibility, as the drastically increased AR results in a slump in D_{core}, which challenges the microfabrication of existing coaxial core lines. Assuming the D_{core} is fixed at the minimally achievable value, the drastically increased AR will require a surge in T_{LC}, resulting in a surge in power consumption and response time (for obtaining the maximally achievable phase shift).

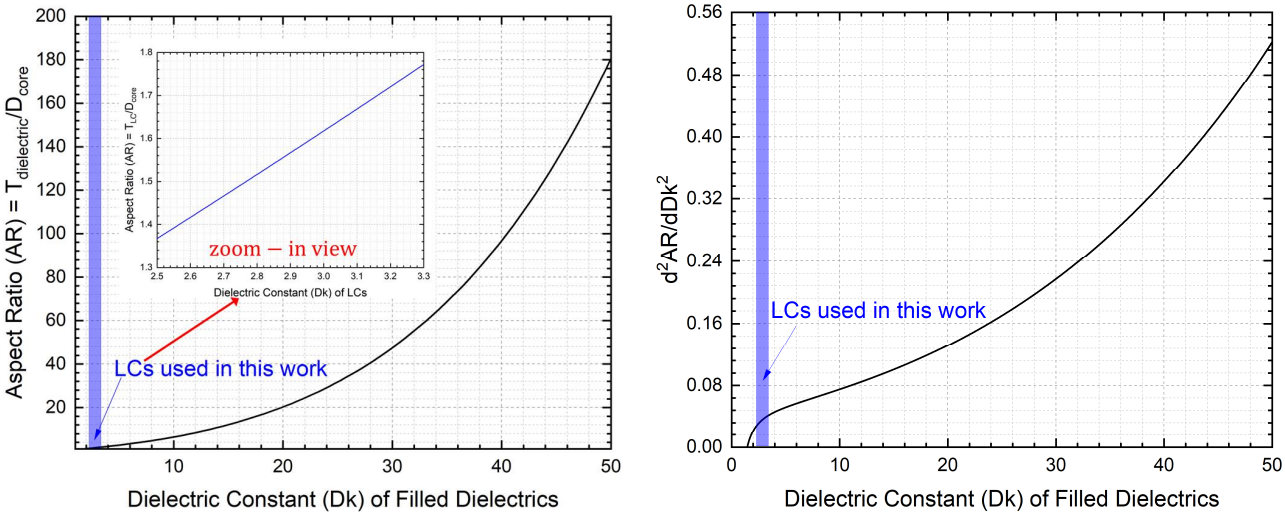

(**a**) (**b**)

Figure 9. 60 GHz analytical results for: (**a**) aspect ratios (ARs) of the coaxial structure for achieving 50 Ω with varied dielectric constants (Dk) between 1 and 50, with a zoomed-in view of our LCs used in this work; (**b**) second-order derivatives of AR to Dk for 50 Ω with varied Dk between 1 and 50.

It is worth noting that the implications obtained here are not constrained to designing LC-filled coaxial reconfigurable devices but also apply to those with other tunable dielectrics, e.g., ferroelectrics and other dielectrics with far higher dielectric constants, for which the manufacturing tolerance and feasibility of the device is deteriorated significantly due to the nonlinearity of AR vs. Dk observed for an extended Dk.

3.2. Effective Permittivity and mmW-PoVR Quantifications

Computationally obtained results of the effective permittivity (ε_{eff}) for the coaxial delay line are compared with the LCs' intrinsic dielectric constant (Dk_{LC}), with their deviation $\Delta\varepsilon$ (governed by Equation (3)), and plotted in Figure 10a below versus the variation of T_{LC}. Correspondingly, the mmW-PoVR of interest is deduced in Figure 10b, as per Equation (4) (raised in Section 2.2).

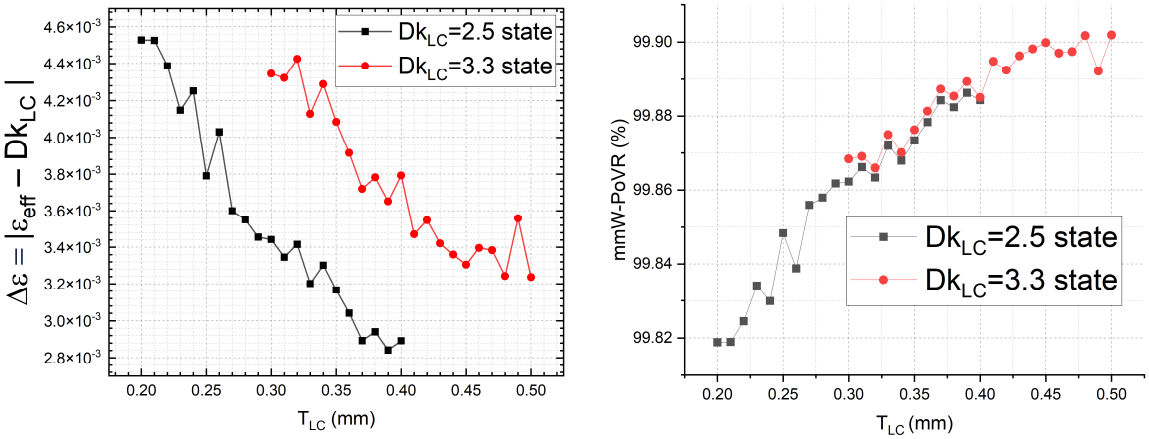

Figure 10. 60 GHz simulation results for: (**a**) deviation between computed effective permittivity of the coaxial delay line device and LCs' intrinsic dielectric constant (macroscopically) at various LC thicknesses; (**b**) derived mmW-PoVR in tunable dielectrics (LCs) of various thicknesses for the coaxial delay line.

As observed in Figure 10a, the deviation of the ε_{eff} prediction (i.e., $\Delta\varepsilon$) reduces with the rise in T_{LC}, i.e., tightly matched with Figure 10b, i.e., the mmW-PoVR is rising towards 99.9% (approaching 100% for the theoretically transverse electromagnetic mode). The delay line filled with LCs where the Dk = 3.3 (saturated bias state) exhibits a slightly higher mmW-PoVR than that with the Dk = 2.5 state (for various T_{LC}). Arguably, the theoretically idealized 100% of mmW-PoVR in LCs holds true for the proposed coaxially structured phase shifter in this work, which indicates the maximally efficient phase shifting geometry possible, as the tuning of the dielectrics is entirely converted to the phase tuning of the delay line without dissipating in any other nontunable dielectrics. As confirmed by the theoretical and simulated results comparison conducted in Figure 10, we have identified a simplified design process for estimating the effective permittivity that can be used to accurately predict the maximum phase shifting range of the proposed LC-filled coaxial phase shifter.

Nevertheless, as mentioned earlier in Sections 2.1 and 2.2, the idealized 100% mmW-PoVR computed for the coaxial delay line with LCs is practically compromised significantly in the achievable tuning range due to the technically demanding alignment process [37] for the nonplanar structure, indicating that the overall merit of the coaxial structure may not surpass other planar structures (e.g., the inverted microstrip [29] and enclosed coplanar waveguide [24]) that exhibit a far lower mmW-PoVR but with a wider achievable tuning range of the material's permittivity. The comparison results among these structures will be quantified and discussed later in Section 3.4.

3.3. Evaluation of Phase Shift and Insertion Loss Variations across Various Tuning States

Phase shifting and insertion loss performance optimization and hence the FoM enhancement at 60 GHz based on the proposed Dk baseline impedance matching approach is investigated, with the parameterization results reported in Figure 11a for the differential phase shift, Figure 11b for the maximum insertion loss, and Figure 12 for the derived FoM. Note that each of the Dks in the horizontal axis corresponds to a specific T_{LC} for 50 Ω, the data of which have been mapped in the contour results shown earlier in Figure 8.

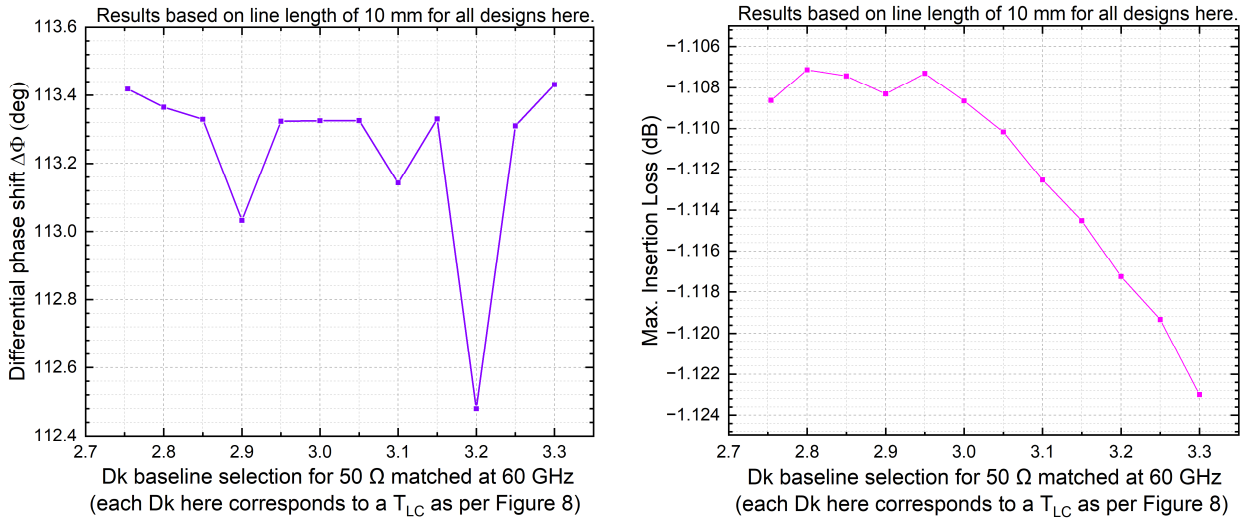

Figure 11. 60 GHz simulation results for (**a**) differential phase shift versus selected Dk baseline for 50 Ω matching of our LC-filled coaxial phase shifter; (**b**) maximum insertion loss versus selected Dk baseline for 50 Ω matching of our LC-filled coaxial phase shifter.

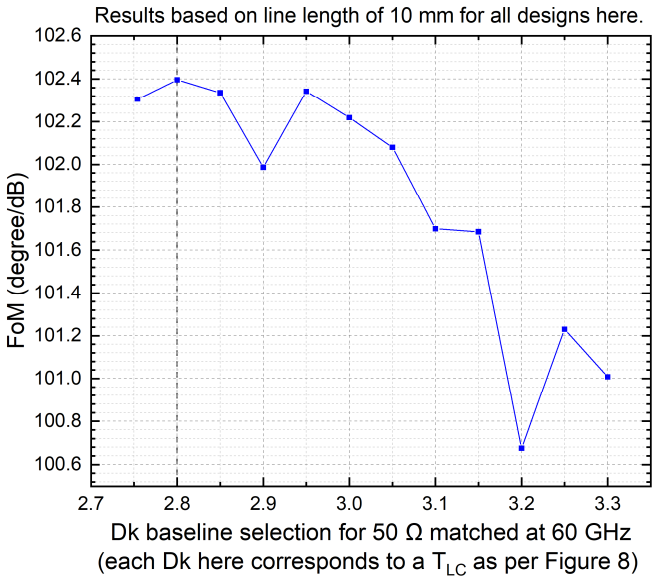

Figure 12. Simulated FoM versus selected Dk baseline for 50 Ω matching of our LC-filled coaxial phase shifter model at 60 GHz.

As observed from Figure 12, the highest FoM is obtained when selecting a Dk of 2.8 (the corresponding T_{LC} of 0.34876 mm) as the baseline for 50 Ω matching. As such, the optimum cross-section geometry is determined as T_{LC} = 0.34876 mm. The line length to meet the maximum differential phase shift requirement of 180° is hence proportionally

derived as 15.92 mm according to Figure 11a. This optimally designed device structure is then simulated across 54 GHz to 66 GHz, with the differential phase shift and insertion loss (at both the most lossy and least lossy states) presented in Figures 13a and 13b, respectively. The proposed loss components decomposition analysis is applied to this optimum structure at 60 GHz, with the results identified in Figure 14 for these two extreme states.

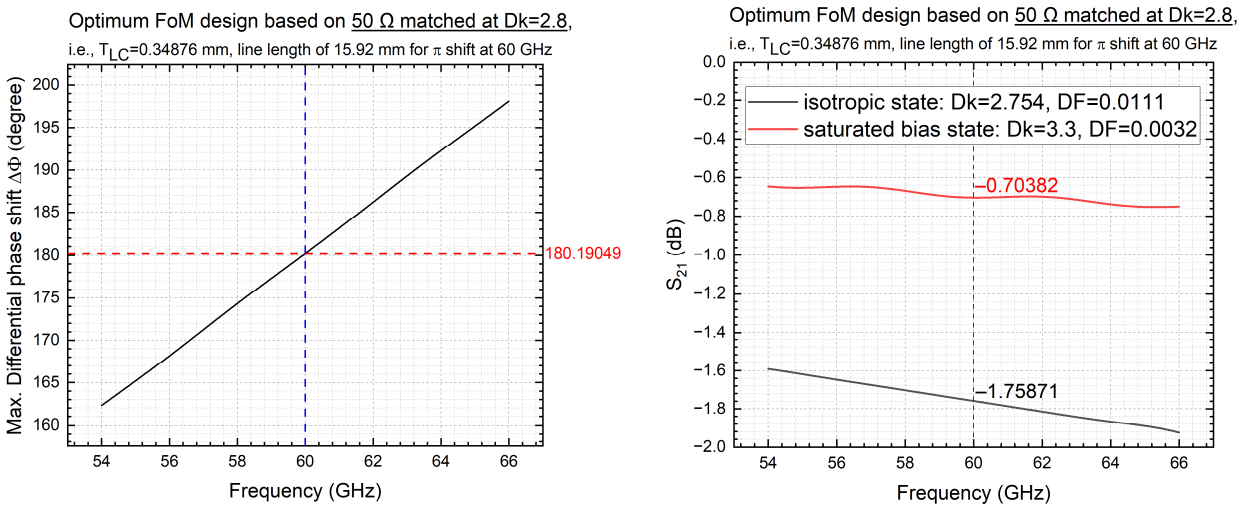

(**a**) (**b**)

Figure 13. Key simulated performance results for the optimally designed LC-filled coaxially structured 0–180° phase shifter (T_{LC} = 0.34876 mm, line length = 15.92 mm): (**a**) maximally achievable differential phase shift versus frequency (54–66 GHz); (**b**) insertion loss versus frequency (54–66 GHz).

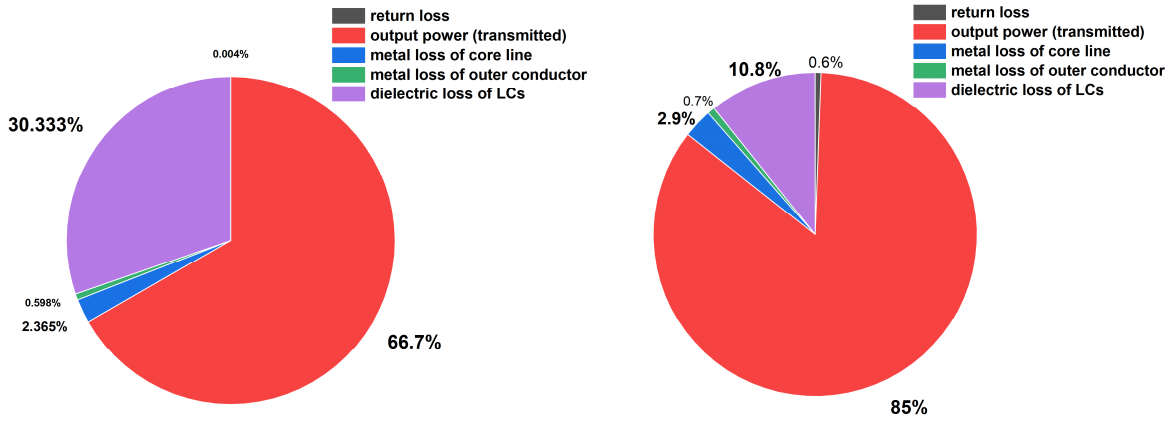

(**a**) (**b**)

Figure 14. Simulated 60 GHz power transmission and dissipation decomposition for the optimized LC-filled coaxially structured 0–180° variable phase shifter design (T_{LC} = 0.34876 mm, line length = 15.92 mm): (**a**) Dk = 2.754 state (LCs at isotropic status); (**b**) Dk = 3.3 state (LCs at saturated bias status).

As observed from Figure 14 regarding the two extreme tuning states, the dielectric loss of LCs dominates for both cases. For the isotropic state where the dielectric dissipation factor (DF) of LCs reaches the maximum (among the workable tuning states of the coaxial structure), the dielectric loss of LCs occupies 30.333%, which overwhelms other loss components (e.g., return loss of 2.365%). There is a slump in this percentage (dielectric loss of LCs) for the saturated bias state (wherein the DF of LCs reaches the minimum), with the dielectric loss of LCs declining to 10.8%.

Note that the metal losses here are idealized by accounting for perfectly patterned surfaces only (i.e., free of roughness). Under this assumption, the core line's metal loss reports 2.365% and 2.9% for the isotropic state and saturated bias state of LCs, respectively. The rise in this figure (for the same geometry but different Dk states) is due to the mmW electric field redistribution, i.e., with the increase in the Dk, mmW power (field intensity) becomes more concentrated (peaking) on the core line's surface. For both states, the outer conductor dissipates less than 1% of the input power due to the far lower mmW field intensity at the outer conductor's inner surface.

3.4. Performance Comparison with Other States-of-the-Art Structures and Discussions

The overall performance comparison is quantified in Table 1, highlighting the proposed LC-filled coaxial topology against other state-of-the-art transmission line structures reported at the same frequency of 60 GHz, using the same grade of LCs (GT3-24002), and meeting the same phase shifting requirement of 0–180° for a relatively fair comparison. The figure of merit (FoM, as defined by Equation (8) in Section 2.4) that represents the trade-off between the maximum phase shifting capability (in degree) and the worst-case (maximum) insertion loss (in dB) is compared. Arguably, the mainstream FoM metric as adopted in Table 1 has imperfections in terms of the effectiveness and fairness regarding devices of different line lengths, the deficiency of which was first raised in our past characterization work [17], for which the interested readers can refer to for delving further into this issue.

Table 1. 60 GHz performance evaluation of various phase shifter device structures filled with the same type of LC (GT3-24002).

Structures	FoM (°/dB)	Line Length (mm)	Workable Range of Dk	PI Requirement (Baking, Rubbing)	CTE * Mismatch Problem
Inverted microstrip model [29]	112.17	13.50	2.5–3.3	Required	Significant
Enclosed coplanar model [24]	109.09	14.32	2.5–3.3	Required	Significant
Enclosed coplanar measured [24]	40.79	15.75	2.5–3.3	Required	Significant
Coaxial model (this work)	102.46	15.92	2.754–3.3	Not required	Minimized

* CTE refers to the coefficient of thermal expansion.

Notably, with the proposed coaxial approach, the conventional LC-filled MW devices fabrication and assembling process (which is time-consuming and cost-prohibitive in materials and clean-room facilities) can be dramatically simplified. To be more specific, the following conventionally key steps can all be eliminated, including the spin-coating of polyimide (PI) as an alignment agent (wherein spin-coater and PI are required), the 200 °C baking of the PI layer for solvent evaporation (time consuming and prone to tarnishing [41] of the plated gold), and the mechanical rubbing of the coated PI (wherein high-precision roller and pressure control systems are required). The removal of the above steps not only significantly speeds up the prototyping, reducing costs (materials and facilities), but also mitigates the vulnerabilities of performance degradation due to fabrication errors and manufacturing tolerances issues, hence improving yields. Furthermore, the thermal issue (which happened during the conventional baking PI step) will be addressed concerning the undesirable tarnishing (oxidized copper migration into the plated gold as observed in our experiments [24,41]) and hence the elevated conductor loss and insertion loss [41]. Instead, there will be no PI and no baking required in this work, i.e., the substrate assembling can be performed at room temperature. Moreover, the removal of PI also contributes to fewer dielectric losses at mmW frequencies, thus reducing insertion loss.

Note that the inverted microstrip by design as we reported [29] does not take into account the PI layer in the computation models, for which the insertion loss and hence FoM performance have been overestimated. As evidenced by our measurement results for our fabricated enclosed coplanar waveguide phase shifter at the same 60 GHz frequency,

the FoM (by measurement) is significantly compromised compared with the designed (predicted) values. Arguably, the PI-related process can play a big part in the elevated insertion loss. Moreover, the recipe of 200 °C baking for the PI processing also leads to a significant mismatch in the coefficients of thermal expansion (CTE) for the multimaterial system that occurred for LC-filled inverted microstrip and enclosed coplanar structures (as per our experimental observation of the substrates' deformation [24] that compromises the flatness of the sandwiched LC layer and causes performance instability in our LC-filled enclosed coplanar phase shifter). For the proposed coaxial topology, the free nature of the PI film processing and hence the removal of the high-temperature baking largely eliminates the CTE-induced deformation concern. Working in harsh environments, the lack of a third constitutive material (i.e., a solid PCB dielectric substrate required in other structures) also largely mitigates the possibility of the CTE mismatch problem. From these observations, the proposed coaxial solution can largely enhance the robustness of the LC mmW phase shifter device, thus expanding the horizons of their potential applications in harsh environments (e.g., space and other mission-critical use cases).

It is worth noting that the results on FoM and line length reported in Table 1 are all based on straight delay lines without meandering the core line. Examining the required line length for achieving the same phase shift of 180°, the coaxial method is 1.6 mm longer than our past enclosed CPW design and 2.42 mm longer than our inverted microstrip solution. This is due to the limited tuning range of the Dk as evidenced in the table for the coaxial one, which overwhelms its advantage in mmW-PoVR as mentioned earlier in Section 2.2. While coaxial is a nonplanar solution, it exhibits the unique property of flexible, conformal circuitry. Future research will thus target a meandering coaxial for ultra-compact solutions.

In terms of frequency scalability, the coaxial method exhibits a plug-and-play design advantage with a replaceable core line of different sizes possible to cater to different operating frequencies. Compatible with industry-standard coaxial connectors at various frequencies (e.g., SMA, 1.85 mm connectors, etc.), the coaxial solution is arguably less challenging in impedance matching than other established structures (e.g., LC-based inverted microstrip, LC-based coplanar-adapted geometries, etc.). Note that the comparison of the modeling results in Table 1 has yet to consider the connectors. Another immediate advantage of using the proposed coaxial structure for the LC delay line device is the mode-mismatch-free property when connectors (coaxial) are installed. Although the coaxial connectors on both sides may exhibit dissimilar dielectrics and geometry size as compared to the LC-filled coaxial delay line, the discontinuity due to this is minimal when compared to the planar structures of the LC delay line (e.g., inverted microstrip [29] and enclosed coplanar [24]) as their interfaced geometries are vastly changed, stimulating higher-order modes, as visualized in [42].

It is also worth noting that decoupling between the low frequency (LF) biasing field and the mmW transmitting field is mandatory if targeting industry-standard product delivery of a phased array system in mission-critical applications, in particular for power-consuming LC-accommodating structures (e.g., waveguides that can normally require high voltage bias beyond 100 V [43–47]). However, for the proof-of-concept standalone device physics characterization stage of LC-based low-power-consuming (e.g., bias voltage up to 20 V [11,24,41]) transmission lines (instead of the power-consuming waveguides [43–47]), the LF-mmW decoupling network is not necessarily needed for the modern generation of vector network analyzers (VNA), wherein a port bias is normally embedded in the VNA for the input of an amplified LF bias signal limited up to 30 V. As such, the complicated decoupling network is not encompassed within our computational modeling frameworks in this work. Nevertheless, for follow-up developments of a real-world phased array feeding system, suitable connector mounting and LF-mmW decoupling network implementation (e.g., by embedding bias tees [48–50], introducing additional biasing networks [51–54], or relying on novel structural mechanisms [55,56]) should be conducted as per the application specifications to address the limitations of the current work's analytical and numerical evaluations. More specifically, the perturbations in the achievable differential phase shift, return

loss, and insertion loss due to the addition of the decoupling network (e.g., bias tees as depicted in Figure 2) will be experimentally quantified as ongoing optimization endeavors.

Grounded in the FoM enhancement achieved by this work, future endeavors will also target the insertion loss balancing by default for beam steering applications, i.e., without external interface control or compensation in amplitude using amplifiers or attenuators that are bulky, complex, and cost-prohibitive. However, this might compromise the conventionally defined FoM. To measure success, a bespoke FoM shall be devised and employed to consider the insertion loss balancing among all tuning states, e.g., a fluctuation factor (FF) can be introduced in the denominator of the updated FoM′ as Equation (12) below:

$$\text{FoM}' = \frac{\Delta\Phi_{\max}}{\text{IL}_{\max} \times \text{FF}}. \tag{12}$$

For other specific applications, cross-disciplinary approaches, and cross-departmental metrics (e.g., flow dynamics [57,58], thermal stability [59,60], resilience, robustness, manufacturability, radiation hardness [61,62], etc.) could be conceived to complement the FoM′ discussion as kicked off from Equation (12). For instance, the ultra-fast response is desired but not a must for certain applications, e.g., space-based radio instrumentation, whereas radiation hardness is mandatory.

4. Concluding Remarks and Outlook

The ongoing 5G services [63–66] and upcoming 6G ecosystem [67–74] will be heavily relying on microwave (MW) and millimeter-wave (mmW) beam steering, for which tunable dielectrics such as liquid crystals (LCs) have been identified as one of the potentially enabling materials for generating continuously variable phase (time) delays electronically to feed antenna arrays passively. As we continue to push the boundaries of mmW technology by exploring its combination possibilities with LCs for efficient reconfigurability, this feasibility study indicates that an LC-based coaxial phase shifter is a promising candidate for expanding the portfolio of existing LC-based reconfigurable devices with an enhanced electromagnetic shielding capability (against instabilities and interference vulnerable at higher-frequency mmW) as well as a simplified manufacturing possibility (lower cost and cycle time).

In recognition of the LC-filled coaxial topology's main limitation on the relatively lower tuning range of the dielectric constant (Dk) per unit length (as compared with planar solutions such as inverted microstrips and enclosed coplanar waveguides), we thus propose to compensate it with a particular focus on exploitable strategies likely to reduce the insertion loss for a decent figure of merit (FoM) that can compete with the established planar solutions. The overarching purpose of the FoM optimization is met in this work by proposing a novel impedance matching baseline approach that examines the most suitable Dk state of LCs for the 50 Ω perfectly matching status, which transfers to the key geometry parameters, i.e., the corresponding thickness of the LC dielectrics (which also defines the distance between the core line and the outer conductor housing). Notably, the device fabrication and assembly processes are envisaged to be free of the conventional polyimide (PI) film as an alignment agent, hence mitigating the conventionally reported PI-induced thermal and electrical concerns. Significant cost reduction and yield improvement can be envisaged for expanded application scenarios in harsh environments.

The coaxial delay line can also be utilized to characterize LCs' dielectric response, i.e., as an integrated dielectric measurement apparatus in addition to a phase shifting/time-delaying device. Existing treatments and predictions are largely based on the two extreme states ($\text{Dk}_{\max}$ and $\text{Dk}_{\min}$) at equilibrium, whereas the intermediate states have yet to be clearly characterized for a wider variety of candidate LC materials at the mmW regime. As such, the topology feasibility study as inspired by this work can serve as a test structure for broadband characterization of LC materials and new electro-optical effects, i.e., exhibiting significant potential to accelerate advanced LC material exploration and design tailored for mmW frequencies and beyond. Last but not least, new opportunities are emerging to

develop data-driven, computationally inexpensive software for automatically designing LC-based coaxial phase shifters to facilitate near-real-time analysis and scaling up analyses for phased array antennas' feed.

Author Contributions: Conceptualization and methodology, J.L.; software, H.L.; validation and formal analysis, J.L. and H.L.; investigation and data curation, J.L. and H.L.; writing—original draft preparation, J.L. and H.L.; writing—review and editing, J.L.; visualization, J.L. and H.L.; supervision, J.L.; project administration and funding acquisition, J.L. All authors have read and agreed to the published version of the manuscript.

Funding: This research was funded by the National Natural Science Foundation of China, grant number 62301043.

Data Availability Statement: Data are available upon request from the corresponding author.

Conflicts of Interest: The authors declare no conflicts of interest. The funders had no role in the design of the study; in the collection, analyses, or interpretation of data; in the writing of the manuscript; or in the decision to publish the results.

References

1. Bonacchini, G.E.; Omenetto, F.G. Reconfigurable microwave metadevices based on organic electrochemical transistors. *Nat. Electron.* **2021**, *4*, 424–428. [CrossRef]
2. Chan, K.Y.; Ramer, R. Millimeter-wave reconfigurable bandpass filters. *Int. J. Microw. Wirel. Technol.* **2015**, *7*, 671–678. [CrossRef]
3. Burasa, P.; Mnasri, B.; Wu, K. Millimeter-Wave CMOS Sourceless Receiver Architecture for 5G-Served Ultra-Low-Power Sensing and Communication Systems. *IEEE Trans. Microw. Theory Tech.* **2019**, *67*, 1688–1696. [CrossRef]
4. Topak, E.; Hasch, J.; Wagner, C.; Zwick, T. A Novel Millimeter-Wave Dual-Fed Phased Array for Beam Steering. *IEEE Trans. Microw. Theory Tech.* **2013**, *61*, 3140–3147. [CrossRef]
5. Giuliano, R.; Mazzenga, F.; Vizzarri, A.; Vegni, A.M. Adaptable Communication System (ACS) for Flexible Communications in the Transport Sector: The AB4Rail project experience. In Proceedings of the 2021 AEIT International Conference on Electrical and Electronic Technologies for Automotive, Torino, Italy, 17–19 November 2021.
6. Uddin, M.R.; Law, F.K.; Jalal, A.H. Design and simulation of an electro-optic even parity bit error detection system. *Opt. Quant. Electron.* **2021**, *53*, 593. [CrossRef]
7. Basharat, S.; Khan, M.; Iqbal, M.; Hashmi, U.S.; Zaidi, S.A.R.; Robertson, I. Exploring reconfigurable intelligent surfaces for 6G: State-of-the-art and the road ahead. *IET Commun.* **2022**, *16*, 1458–1474. [CrossRef]
8. Sanjari, P.; Aflatouni, F. An integrated photonic-assisted phased array transmitter for direct fiber to mm-wave links. *Nat Commun.* **2023**, *14*, 1414. [CrossRef] [PubMed]
9. Trzebiatowski, K.; Rzymowski, M.; Kulas, L.; Nyka, K. Simple Millimeter Wave Identification System Based on 60 GHz Van Atta Arrays. *Sensors* **2022**, *22*, 9809. [CrossRef] [PubMed]
10. Rzaik, N.; Dehos, C.; Zarudniev, M.; Siligaris, A.; Gonzalez, J.L.J. A mmW RadCom System for Short-Range Hand Gesture Sensing and Data Synchronization. In Proceedings of the 2023 18th Conference on Ph.D Research in Microelectronics and Electronics, Valencia, Spain, 18–21 June 2023.
11. Li, J. Millimetre-wave beam steering with analog-resolution and minimised distortion based on liquid crystals tunable delay lines with enhanced signal-to-noise ratios. In *Millimetre Wave and Terahertz Sensors and Technology XIII*; SPIE: Bellingham, WA, USA, 2020; Volume 11541, pp. 68–73.
12. Zaid, F.N.M.; Azemi, S.N.; Beson, M.R.C. Application of FSS for Microstrip Antenna for Gain Enhancement. *IOP Conf. Ser.* **2020**, *767*, 012001. [CrossRef]
13. Hirabayashi, K.; Wada, M.; Amano, C. Liquid crystal variable optical attenuators integrated on planar lightwave circuits. *IEEE Photonics Technol. Lett.* **2001**, *13*, 609–611. [CrossRef]
14. Arshad, F.; Ahmad, A.; Amin, Y.; Abbasi, M.A.B.; Choi, D.Y. MIMO antenna array with the capability of dual polarization reconfiguration for 5G mm-wave communication. *Sci. Rep.* **2022**, *12*, 18298. [CrossRef]
15. Asfour, R.; Khamas, S.K.; Ball, E.A. Cost-Effective Design of Polarization and Bandwidth Reconfigurable Millimeter-Wave Loop Antenna. *Sensors* **2023**, *23*, 9628. [CrossRef]
16. Qamar, Z.; Zheng, S.Y.; Chan, W.S.; Ho, D. An Equal-Length Multiway Differential Metamaterial Phase Shifter. *IEEE Trans. Microw. Theory Tech.* **2017**, *65*, 136–146. [CrossRef]
17. Li, J. Rethinking Figure-of-Merits of Liquid Crystals Shielded Coplanar Waveguide Phase Shifters at 60 GHz. *J* **2021**, *4*, 444–451. [CrossRef]
18. Abdulazhanov, S.; Le, Q.H.; Huynh, D.K.; Wang, D.; Gerlach, G.; Kämpf, T. A mmWave Phase Shifter Based on Ferroelectric Hafnium Zirconium Oxide Varactors. In Proceedings of the 2019 IEEE MTT-S International Microwave Workshop Series on Advanced Materials and Processes for RF and THz Applications, Bochum, Germany, 16–18 July 2019; pp. 175–177.

19. Sohn, I.B.; Choi, H.K.; Noh, Y.C.; Kim, J.; Ahsan, M.S. Laser assisted fabrication of micro-lens array and characterization of their beam shaping property. *Appl. Surf. Sci.* **2019**, *479*, 375–385. [CrossRef]
20. Uddin, M.R.; Wallner, J.; Dikshit, A.; Hossain, M.J.; Timalsina, Y.; Fahrenkopf, N.M.; Harame, D.L. Cascaded ring resonator based wide stop-band filter fabricated in AIM photonics technology at Albany Nanotech Complex. *Proc. SPIE* **2023**, *12424*, 124240U.
21. Choi, H.K.; Jung, Y.J.; Yu, B.A.; Sung, J.H.; Sohn, I.B.; Kim, J.Y.; Ahsan, M.S. Femtosecond-Laser-Assisted Fabrication of Radiation-Resistant Fiber Bragg Grating Sensors. *Appl. Sci.* **2022**, *12*, 886. [CrossRef]
22. Outram, B. Nematic liquid crystals. In *Liquid Crystals*, 1st ed.; IOP Publishing: Bristol, UK, 2018; Volume 4, pp. 1–14.
23. Muller, S.; Scheele, P.; Weil, C.; Wittek, M.; Hock, C.; Jakoby, R. Tunable passive phase shifter for microwave applications using highly anisotropic liquid crystals. In Proceedings of the IEEE MTT-S International Microwave Symposium Digest, Fort Worth, TX, USA, 6–11 June 2004; pp. 1153–1156.
24. Li, J.; Chu, D. Liquid Crystal-Based Enclosed Coplanar Waveguide Phase Shifter for 54–66 GHz Applications. *Crystals* **2019**, *9*, 650. [CrossRef]
25. Mueller, S.; Goelden, F.; Scheele, P.; Wittek, M.; Hock, C.; Jakoby, R. Passive Phase Shifter for W-Band Applications using Liquid Crystals. In Proceedings of the 2006 European Microwave Conference, Manchester, UK, 10–15 September 2006; pp. 306–309.
26. Reese, R.; Polat, E.; Tesmer, H.; Strobl, J.; Schuster, C.; Nickel, M.; Granja, A.B.; Jakoby, R.; Maune, H. Liquid Crystal Based Dielectric Waveguide Phase Shifters for Phased Arrays at W-Band. *IEEE Access* **2019**, *7*, 127032–127041. [CrossRef]
27. Hähsler, M.; Nádasi, H.; Feneberg, M.; Marino, S.; Giesselmann, F.; Behrens, S.; Eremin, A. Magnetic Tilting in Nematic Liquid Crystals Driven by Self-Assembly. *Adv. Funct. Mater.* **2021**, *31*, 2101847. [CrossRef]
28. Yazdanpanahi, M.; Syahkal, D.M. Millimeter-wave liquid-crystal-based tunable bandpass filter. In Proceedings of the 2012 IEEE Radio and Wireless Symposium, Santa Clara, CA, USA, 15–18 January 2012; pp. 139–142.
29. Li, J. Rethinking Liquid Crystal Tunable Phase Shifter Design with Inverted Microstrip Lines at 1–67 GHz by Dissipative Loss Analysis. *Electronics* **2023**, *12*, 421. [CrossRef]
30. Christou, M.A.; Papanicolaou, N.C.; Polycarpou, A.C. A nematic liquid crystal tunable patch antenna. In Proceedings of the 8th European Conference on Antennas and Propagation (EuCAP 2014), Hague, The Netherlands, 6–11 April 2014; pp. 1875–1878.
31. Nobles, J.E.; Smiley, K.; Baques, D.B.; Economou, E.; Herman, J.; Harward, I.; Glushchenko, A.; Camley, R.E.; Celinski, Z. Eight-element liquid crystal based 32 GHz phased array antenna with improved time response. *Eng. Res. Express* **2021**, *3*, 045033. [CrossRef]
32. Li, J. Novel Partially-Shielded Coplanar Waveguide with Metasurfaces for Liquid Crystals Tunable Delay Lines Beyond 67 GHz. In Proceedings of the 2022 IEEE Conference on Antenna Measurements & Applications (IEEE CAMA), Guangzhou, China, 14–17 December 2022; pp. 1–4.
33. Li, J. 79 GHz Meandering Enclosed-Coplanar Variable Delay Lines in Liquid Crystals Encapsulated Within Independent and Shared Cavities. In Proceedings of the IEEE 27th International Symposium on Antennas and Propagation (ISAP), Sydney, Australia, 31 October–3 November 2022; pp. 457–458.
34. Li, J. 60 GHz 0-360° Passive Analog Delay Line in Liquid Crystal Technology based on a Novel Conductor-backed Fully-enclosed Coplanar Waveguide. In Proceedings of the 2022 IEEE 72nd Electronic Components and Technology Conference (ECTC), San Diego, CA, USA, 31 May–3 June 2022; pp. 1841–1846.
35. Heekwon, L.; Soojung, R.; Seungbae, L.; Kim, S.; Nah, W. Electromagnetic Field Interference on Transmission Lines due to On-Board Antenna. *Int. J. Antennas Propag.* **2015**, *2015*, 104506.
36. Li, J. Will 'Liquid-Crystal-Based Floating-Electrode-Free Coplanar Waveguide Phase Shifter with an Additional Liquid-Crystal Layer for 28-GHz Applications' Work? " *Eng. Lett.* **2023**, *31*, 820–824.
37. Li, J.; Xu, H.; Chu, D. Design of liquid crystal based coplanar waveguide tunable phase shifter with no floating electrodes for 60–90 GHz applications. In Proceedings of the 2016 46th European Microwave Conference (EuMC), London, UK, 4–6 October 2016; pp. 1047–1050.
38. Dhruvakumar, T.; Chaturvedi, A. Intelligent Reflecting Surface assisted millimeter wave communication for achievable rate and coverage enhancement. *Veh. Commun.* **2022**, *33*, 100431. [CrossRef]
39. Jost, M.; Strunck, S.; Heunisch, A.; Wiens, A.; Prasetiadi, A.E.; Weickhmann, C.; Schulz, B.; Quibeldey, M.; Karabey, O.H.; Rabe, T.; et al. Continuously tuneable liquid crystal based stripline phase shifter realised in LTCC technology. In Proceedings of the 2015 European Microwave Conference (EuMC), Paris, France, 7–10 September 2015; pp. 1260–1263.
40. Alloatti, L.; Pfeifle, J.; Mendez, J.; Freude, W.; Leuthold, J.; Koos, C. Liquid crystal phase shifter on the SOH platform with ultra-low power consumption. In Proceedings of the OFC/NFOEC, Los Angeles, CA, USA, 4–8 March 2012; pp. 1–3.
41. Li, J. 60 GHz Optimised Nickel-free Gold-plated Enclosed Coplanar Waveguide Liquid Crystal Phase Shifter. In Proceedings of the 2020 IEEE MTT-S International Microwave Workshop Series on Advanced Materials and Processes for RF and THz Applications (IMWS-AMP), Suzhou, China, 29–31 July 2020; pp. 1–3.
42. Li, J. Wideband PCB-to-Connectors Impedance Adapters for Liquid Crystal-Based Low-Loss Phase Shifters. In Proceedings of the 50th European Microwave Conference (EuMC), Utrecht, The Netherlands, 12–14 January 2021; pp. 546–549.
43. Reese, R.; Polat, E.; Jost, M.; Nickel, M.; Jakoby, R.; Maune, H. Liquid crystal based phase shifter in a parallel-plate dielectric waveguide topology at V-band. In Proceedings of the 2017 12th European Microwave Integrated Circuits Conference (EuMIC), Nuremberg, Germany, 8–10 October 2017; pp. 353–356.

44. Polat, E.; Reese, R.; Jost, M.; Nickel, M.; Schuster, C.; Jakoby, R.; Maune, H. Liquid Crystal Phase Shifter Based on Nonradiative Dielectric Waveguide Topology at W-Band. In Proceedings of the 2019 IEEE MTT-S International Microwave Symposium (IMS), Boston, MA, USA, 2–7 June 2019; pp. 184–187.
45. Reese, R.; Jost, M.; Maune, H.; Jakoby, R. Design of a continuously tunable W-band phase shifter in dielectric waveguide topology. In Proceedings of the 2017 IEEE MTT-S International Microwave Symposium (IMS), Honololu, HI, USA, 4–9 June 2017; pp. 180–183.
46. Hu, W.; Jiang, D.; Zhang, W.; Liu, Y.; Zhu, K.; Zhang, T. Design of a W-Band Dielectric Phase Shifter Based on Liquid Crystal. *Int. J. Antennas Propag.* **2022**, *2022*, 6486628.
47. Jost, M.; Weickhmann, C.; Strunck, S.; Gäbler, A.; Fritzsch, C.; Karabey, O.H.; Jakoby, R. Liquid crystal based low-loss phase shifter for W-band frequencies. *Electron. Lett.* **2013**, *49*, 1460–1462. [CrossRef]
48. Nova, V.; Bachiller, C.; Villacampa, B.; Kronberger, R.; Boria, V.E. Characterization of Nematic Liquid Crystals at Microwave Frequencies. *Crystals* **2020**, *10*, 1106. [CrossRef]
49. Christie, S.; Cahill, R.; Mitchell, N.; Munro, Y.; Manabe, A. Electronically scanned Rotman lens antenna with liquid crystal phase shifters. *Electron. Lett.* **2013**, *49*, 445–447. [CrossRef]
50. Cai, L.; Chu, D. Compact liquid crystal based phase shifter with integrated bias tees. In Proceedings of the 2018 IEEE MTT-S International Wireless Symposium (IWS), Chengdu, China, 6–10 May 2018; pp. 1–4.
51. Prasetiadi, A.E.; Karabey, O.H.; Weickhmann, C.; Franke, T.; Hu, W.; Jost, M.; Nickel, M.; Jakoby, R. Continuously tunable substrate integrated waveguide bandpass filter in liquid crystal technology with magnetic biasing. *Electron. Lett.* **2015**, *51*, 1584–1585. [CrossRef]
52. Li, X.; Sato, H.; Shibata, Y.; Ishinabe, T.; Fujikake, H.; Chen, Q. Development of Beam Steerable Reflectarray with Liquid Crystal for Both E-Plane and H-Plane. *IEEE Access* **2022**, *10*, 26177–26185. [CrossRef]
53. Polat, E.; Tesmer, H.; Reese, R.; Nickel, M.; Wang, D.; Schumacher, P.; Jakoby, R.; Maune, H. Reconfigurable Millimeter-Wave Components Based on Liquid Crystal Technology for Smart Applications. *Crystals* **2020**, *10*, 346. [CrossRef]
54. Wang, Q.; Su, Z.; Li, S.; Zhao, H.; Yin, X. Electrically tunable liquid crystal phase shifter with excellent phase shift capability per wavelength based on opposed coplanar waveguide. *J. Phys. D Appl. Phys.* **2022**, *55*, 405001. [CrossRef]
55. Polat, E.; Kamrath, F.; Matic, S.; Tesmer, H.; Jiménez-Sáez, A.; Wang, D.; Maune, H.; Höft, M.; Jakoby, R. Novel Hybrid Electric/Magnetic Bias Concept for Tunable Liquid Crystal Based Filter. *IEEE J. Microw.* **2022**, *2*, 490–495. [CrossRef]
56. Nickel, M.; Jiménez-Sáez, A.; Agrawal, P.; Gadallah, A.; Malignaggi, A.; Schuster, C.; Reese, R.; Tesmer, H.; Polat, E.; Wang, D.; et al. Ridge Gap Waveguide Based Liquid Crystal Phase Shifter. *IEEE Access* **2020**, *8*, 77833–77842. [CrossRef]
57. Kinoshita, Y.; Uchida, N. Flow patterns and defect dynamics of active nematic liquid crystals under an electric field. *Phys. Rev. E* **2023**, *108*, 014605. [CrossRef] [PubMed]
58. Hieber, M.; Nesensohn, M.; Prüss, J.; Schade, K. Dynamics of nematic liquid crystal flows: The quasilinear approach. *Ann. Inst. Henri Poincare (C) Anal. Non Lineaire* **2016**, *33*, 397–408. [CrossRef]
59. Attila, A. Stability of nematic liquid crystals under a temperature gradient. Calculations for PAA. *Int. J. Eng. Sci.* **1976**, *14*, 259–271.
60. Bouriche, A.; Alachaher-Bedjaoui, L.; Barrera, A.; Staelens, J.N.; Maschke, U. Thermal Degradation Studies of Poly(2-ethyl hexyl acrylate) in the Presence of Nematic Liquid Crystals. *Polymers* **2023**, *15*, 3934. [CrossRef] [PubMed]
61. Woehrle, C.D.; Doyle, D.T.; Lane, S.A.; Christodoulou, C.G. Space Radiation Environment Testing of Liquid Crystal Phase Shifter Devices. *IEEE Antennas Wirel. Propag. Lett.* **2015**, *15*, 1923–1926. [CrossRef]
62. Gaebler, A.; Moessinger, A.; Goelden, F.; Manabe, A.; Goebel, M.; Follmann, R.; Koether, D.; Modes, C.; Kipka, A.; Deckelmann, M.; et al. Liquid Crystal-Reconfigurable Antenna Concepts for Space Applications at Microwave and Millimeter Waves. *Int. J. Antennas Propag.* **2009**, *2009*, 876989. [CrossRef]
63. Nestoros, M.; Papanicolaou, N.C.; Polycarpou, A.C. Design of beam-steerable array for 5G applications using tunable liquid crystal phase shifters. In Proceedings of the 2019 13th European Conference on Antennas and Propagation (EuCAP), Krakow, Poland, 31 March–5 April 2019; pp. 1–4.
64. Jakoby, R.; Gaebler, A.; Weickhmann, C. Microwave liquid crystal enabling technology for electronically steerable antennas in SATCOM and 5G millimeter-wave systems. *Crystals* **2020**, *10*, 514. [CrossRef]
65. Camacho-Gomez, C.; Sanchez-Montero, R.; Martínez-Villanueva, D.; López-Espí, P.L.; Salcedo-Sanz, S. Design of a Multi-Band Microstrip Textile Patch Antenna for LTE and 5G Services with the CRO-SL Ensemble. *Appl. Sci.* **2020**, *10*, 1168. [CrossRef]
66. Doré, J.B.; Belot, D.; Mercier, E.; Bicaïs, S.; Gougeon, G.; Corre, Y.; Miscopein, B.; Kténas, D.; Strinati, E.C. Technology Roadmap for Beyond 5G Wireless Connectivity in D-band. In Proceedings of the 2020 2nd 6G Wireless Summit (6G SUMMIT), Levi, Finland, 17–20 March 2020; pp. 1–5.
67. Wang, C.X.; You, X.; Gao, X.; Zhu, X.; Li, Z.; Zhang, C.; Wang, H.; Huang, Y.; Chen, Y.; Haas, H.; et al. On the Road to 6G: Visions, Requirements, Key Technologies, and Testbeds. *IEEE Commun. Surv. Tutor.* **2023**, *25*, 905–974. [CrossRef]
68. Mourad, A.; Yang, R.; Lehne, P.H.; De La Oliva, A. A Baseline Roadmap for Advanced Wireless Research Beyond 5G. *Electronics* **2020**, *9*, 351. [CrossRef]
69. Dangi, R.; Choudhary, G.; Dragoni, N.; Lalwani, P.; Khare, U.; Kundu, S. 6G Mobile Networks: Key Technologies, Directions, and Advances. *Telecom* **2023**, *4*, 836–876. [CrossRef]

70. Jiang, W.; Han, B.; Habibi, M.A.; Schotten, H.D. The Road Towards 6G: A Comprehensive Survey. *IEEE Open J. Commun. Soc.* **2021**, *2*, 334–366. [CrossRef]
71. Bhat, J.R.; Alqahtani, S.A. 6G Ecosystem: Current Status and Future Perspective. *IEEE Access* **2021**, *9*, 43134–43167. [CrossRef]
72. De Alwis, C.; Kalla, A.; Pham, Q.V.; Kumar, P.; Dev, K.; Hwang, W.J.; Liyanage, M. Survey on 6G Frontiers: Trends, Applications, Requirements, Technologies and Future Research. *IEEE Open J. Commun. Soc.* **2021**, *2*, 836–886. [CrossRef]
73. Penttinen, J.T.J. On 6G Visions and Requirements. *J. ICT Stand.* **2021**, *9*, 311–325. [CrossRef]
74. Kumar, R.; Gupta, S.K.; Wang, H.C.; Kumari, C.S.; Korlam, S.S.V.P. From Efficiency to Sustainability: Exploring the Potential of 6G for a Greener Future. *Sustainability* **2023**, *15*, 16387. [CrossRef]